Available online at www.sciencedirect.com
ScienceDirect
Comput. Methods Appl. Mech. Engrg. 299 (2016) 381–400
Computer methods in applied mechanics and engineering
www.elsevier.com/locate/cma

Nodally integrated implicit gradient reproducing kernel particle method for convection dominated problems

Michael Hillman, Jiun-Shyan Chen*

Department of Structural Engineering, University of California, San Diego, 9500 Gilman Drive, La Jolla, CA 92093-0085, United States

Received 14 February 2015; received in revised form 20 October 2015; accepted 2 November 2015
Available online 2 December 2015

Highlights

- A general framework for SU/PG, G/LS, and SGS stabilization methods.
- Equivalence between reproducing kernel implicit gradient and diffuse derivative.
- Stabilized lower order quadrature scheme for convection dominated problems.

Abstract

Convective transport terms in Eulerian conservation laws lead to numerical instability in the solution of Bubnov–Galerkin methods for these non-self-adjoint PDEs. Stabilized Petrov–Galerkin methods overcome this difficulty, however gradient terms are required to construct the test functions, which are typically expensive for meshfree methods. In this work, the implicit gradient reproducing kernel particle method is introduced which avoids explicit differentiation of test functions. Stabilization is accomplished by including gradient terms in the reproducing condition of the reproducing kernel approximation. The proposed method is computationally efficient and simplifies stabilization procedures. It is also shown that the implicit gradient resembles the diffuse derivative originally introduced in the diffuse element method in Nayroles et al. (1992), and maintains the desirable properties of the full derivative. Since careful attention must be paid to efficiency of domain integration in meshfree methods, nodal integration is examined for this class of problems, and a nodal integration method with enhanced accuracy and stability is introduced. Numerical examples are provided to show the effectiveness of the proposed method for both steady and transient problems.

Keywords: Convection dominated problems; Reproducing kernel particle method; Implicit gradient; Stabilization; Nodal integration

1. Introduction

It is well known that the application of standard Bubnov–Galerkin methods to convection dominated problems yields oscillatory solutions. Convective transport terms in Eulerian conservation laws lead to numerical instability in the solution of these problems, and the instability manifests when fine-scale features such as boundary layers

* Corresponding author.
E-mail address: js-chen@ucsd.edu (J.-S. Chen).

http://dx.doi.org/10.1016/j.cma.2015.11.004
0045-7825/

are present in the solution. Stabilized Petrov–Galerkin methods [1–3] have been developed which provide superior stability over standard Bubnov–Galerkin methods. Alternatively, methods that either directly or indirectly include fine-scale features such as the variational multiscale method [4,5], residual free bubbles [6], or subgrid scale (SGS) methods [7], have been introduced to resolve the issue with using Galerkin methods for this class of problems. These two approaches are intimately related, and the motivation and interpretation of each is not necessarily mutually exclusive (cf. [4,5,7–9]).

Stabilized methods predate both bubble methods and variational multiscale methods, although the relationship between the three was later shown in [4]. In these methods, portions of the differential operator are included in the test function, which can be shown to ensure stability of the Galerkin solution with the proper selection of a stabilization parameter. The streamline upwind Petrov–Galerkin (SU/PG) method first presented in [1] gave stabilization in a consistent manner, and put to rest notions of artificial diffusion. Thereafter, an analysis of SU/PG was given in [10] and the Galerkin/least squares (G/LS) method [2] was introduced to give a method grounded in stability and convergence. The SGS stabilized finite element method [11,3] reveals that static condensation of bubble functions is equivalent to the use of the negative adjoint operator for a stabilized method. The stability and convergence of the stabilized finite element methods have been well investigated [10,2,3].

The difficulties with convection dominated problems and methods used to address them discussed above are largely applicable to meshfree methods. In addition, due to the unique properties of these discretizations, several novel approaches have been taken to address the issue apart from traditional stabilization. Early on, the multi-resolution reproducing kernel particle method (RKPM) [12] was introduced to resolve internal layers in the advection–diffusion equation. The finite point method [13,14] employed characteristics to obtain a stable solution. The meshless local Petrov–Galerkin method has also been developed for convection dominated problems in [15,16], with upwinding schemes for the trial functions and local sub-domains. Several more traditional approaches have also been proposed for meshfree methods. Stabilized RKPM [17] has been applied to flow problems, and suitable stabilization parameters have been discussed in [18,19]. A higher order accurate time integration scheme [20] has been proposed for meshfree methods for convection dominated problems. Recently, the variational multiscale framework has been applied to RKPM for convection dominated problems and other related problems in [21–24], using discrete representations of the fine scales.

An ever-present issue in Galerkin meshfree methods is domain integration. Due to the rational nature of shape functions, and often misaligned supports and integration cells, computationally demanding high order integration is often required for solution accuracy [25]. One approach that has been taken is to impose exactness in the Galerkin solution with quadrature. A stabilized conforming nodal integration (SCNI) was proposed in [26,27], which constructs smoothed gradients such that the linear patch test is satisfied, attaining optimal convergence for linear basis. More recently, this concept has been cast under a framework of variational consistency conditions in [28], where it was shown that by constructing gradients such that higher order patch tests are satisfied, optimal convergence rates associated with the order of the approximation space can be attained. Adding additional stress points in a variationally consistent manner has also been proposed to either facilitate higher order accuracy when additional enrichment functions are present [29], or increase the stability of variationally consistent methods [30,31]. In both cases, maintaining variational consistency has been the key to their overall effectiveness.

Implicit gradients have been introduced for meshfree methods for various purposes. The basic idea is to embed the desirable properties of the derivatives in the approximation, e.g., partition of nullity, but do so without differentiating the shape functions. The first use of implicit gradients was for synchronized convergence in [32,33], where it was shown that the approach could also be used as a way to avoid taking derivatives and thus attain efficiency. Implicit gradients have also been used for regularization in strain localization problems [34] to avoid the need of ambiguous boundary conditions associated with the standard gradient-type regularization methods. In [35], they were utilized for easing the computational cost of meshfree collocation methods, which require higher order derivatives. In this paper, the implicit gradient reproducing kernel particle method (IG-RKPM) is introduced for convection dominated problems. A gradient reproducing condition is employed which allows stabilization under a unified framework without the explicit construction of costly gradient terms. The technique is thus computationally efficient, simplifies stabilization procedures considerably, and it requires only a small modification to the standard shape RKPM function. Since the choice of domain integration is critical for meshfree methods to be effective, SCNI is investigated for convection dominated problems. It is shown that while stable when solving self-adjoint equations, it can yield unstable solutions for this class of problems, exhibiting the instability it was originally designed to preclude. As such, high order SCNI

(HSCNI) is introduced for convection dominated problems, which is shown to restore stability while maintaining variational consistency.

The remainder of this paper is as follows. Section 2 reviews the fundamental numerical difficulties associated with convection dominated problems, and common methods for stabilization. The implicit gradient reproducing kernel particle method is then introduced in Section 3, and HSCNI for convection dominated problems is introduced in Section 4. In Section 5, several numerical examples are given, showing the effectiveness of the proposed method in both steady and transient problems. Concluding remarks are then given in Section 6.

2. Review of stabilization for convection dominated problems

2.1. Advection–diffusion equation

The advection–diffusion equation is considered herein as a model problem for convection dominated problems. The strong form asks to find $u(t, \mathbf{x})$ such that

$$\begin{aligned} &\dot{u} + \mathcal{L}u = s \quad \text{in } \Omega \times]0, T[\\ &u(0, \mathbf{x}) = u_0(\mathbf{x}) \quad \forall \mathbf{x} \in \Omega \\ &u = g \quad \text{on } \partial\Omega_g \times]0, T[\\ &\mathcal{B}u = h \quad \text{on } \partial\Omega_h \times]0, T[\end{aligned} \tag{1}$$

where $\dot{u} = \partial u / \partial t$, s is a source term, $\partial\Omega_g$ and $\partial\Omega_h$ are the essential and natural boundaries of the domain, respectively, the flux boundary conditions $\mathcal{B}u = k\nabla u \cdot \mathbf{n}$ are considered, and with constant isotropic diffusion and a divergence-free advection field, the operator $\mathcal{L}$ in (1) is

$$\mathcal{L} = -k\nabla^2 + \mathbf{a} \cdot \nabla \tag{2}$$

where $\mathbf{a}$ and k are the given advection velocity and diffusivity, respectively.

The weak form of (1) is to find $u \in U$ such that for all $w \in W$ the following equation holds:

$$(w, \dot{u})_\Omega + a(w, u) = (w, s)_\Omega + (w, h)_{\partial\Omega_h} \tag{3}$$

where U and W are Sobolev spaces of degree one with proper essential boundary conditions satisfied, $(\cdot, \cdot)_\Omega$ and $(\cdot, \cdot)_{\partial\Omega_h}$ denote the L^2 inner product on the domain and natural boundary respectively, and

$$a(w, u) = (k\nabla w, \nabla u)_\Omega + (w, \mathbf{a} \cdot \nabla u)_\Omega. \tag{4}$$

The Galerkin form of the problem considers finite dimensional subspaces $U^h \subset U$ and $W^h \subset W$, and solves for $u^h \in U^h$ such that for all $w^h \in W^h$ the following holds:

$$(w^h, \dot{u}^h)_\Omega + a(w^h, u^h) = (w^h, s)_\Omega + (w^h, h)_{\partial\Omega_h}. \tag{5}$$

To illustrate the difficulty in applying the Bubnov–Galerkin method to problems such as (1), we first consider the one-dimensional nonhomogeneous steady version, with constant ratio of scalar parameters $a/k = 20.0$, and $s = 0.0$. The problem is solved with the RKPM method, along with linear finite elements for illustration. The length of the domain is chosen as ten, with twenty-one nodes for both the finite element method and RKPM giving a grid Péclet number $Pe_h = \|\mathbf{a}\| h/2k = 5$, greater than what is expected for problems with the boundary layer which can appear in the solution of the model problem (1). Linear basis is employed in the RKPM method with a quartic B-spline kernel and a normalized support of two. As seen in Fig. 1, both methods give oscillatory solutions. While it is well known that standard finite element methods encounter difficulty in convection dominated problems, it is clear from the figure that this is also true for meshfree methods. A general remedy is to enhance the stability of the solution using a stabilized Petrov–Galerkin formulation.

2.2. Stabilized methods

When boundary layers corrupt the numerical solution of convection dominated problems, an intuitive understanding of the instability is the inability of the discretization to capture the fine-scale features of the problem, since

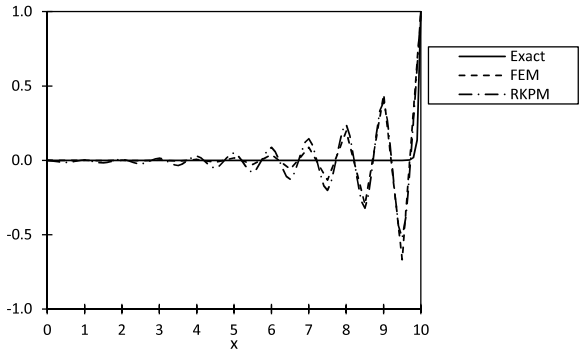

Fig. 1. Oscillatory behavior in Bubnov–Galerkin FEM and RKPM applied to the steady advection–diffusion equation with $Pe_h = 5$.

sufficiently fine discretizations do not suffer from the instability. Under the variational multiscale framework, the fine-scale behavior can be included in the steady Dirichlet version of (5), as in [4]:

$$a(w^h, u^h) + (\tau \mathbb{L} w^h, \mathcal{L} u^h - s)_\Omega = (w^h, s)_\Omega \quad \forall\, w^h \in W^h \tag{6}$$

where τ is a stabilization parameter, and the operator $\mathbb{L}$ varies for each stabilized method:

$$\begin{aligned} &\mathbb{L} = \mathcal{L}_{\text{adv}} \quad \text{SU/PG [1]} \\ &\mathbb{L} = \mathcal{L} \quad \text{G/LS [2]} \\ &\mathbb{L} = -\mathcal{L}^* \quad \text{SGS [3]}. \end{aligned} \tag{7}$$

In the above, $\mathcal{L}^* = -k\nabla^2 - \mathbf{a} \cdot \nabla$ is the adjoint of $\mathcal{L}$ and $\mathcal{L}_{\text{adv}} = \mathbf{a} \cdot \nabla$ is the advective portion of $\mathcal{L}$. Using (6) the three methods SU/PG, G/LS, and SGS can be phrased in terms of the original problem (5) with a modification to the Bubnov–Galerkin test function that takes the familiar form of stabilized methods, which can be expressed in a unified fashion as:

$$\tilde{w}^h = w^h + \tau \mathbb{L} w^h. \tag{8}$$

The stabilized Galerkin method finds $u^h \in U^h \subset U$ such that for all $\tilde{w}^h \in W^h \subset W$ the following holds:

$$(\tilde{w}^h, \dot{u}^h)_\Omega + a(\tilde{w}^h, u^h) = (\tilde{w}^h, s)_\Omega + (\tilde{w}^h, h)_{\partial \Omega_h}, \tag{9}$$

where in this case, proper construction of stabilization requires higher degrees of Sobolev spaces U and W. The regularity requirement is straightforwardly accomplished with meshfree methods, but in contrast, in the finite element method, several stabilization terms are typically neglected, which can result in decreased convergence rates [20].

To illustrate the effectiveness of increasing stability by (8), the RKPM method is employed with the same discretization as the previous example, but now using SU/PG stabilization, and the result is shown in Fig. 2. It can be seen that the oscillations that were present in the RKPM solution are virtually eliminated with stabilization. Here, the classical stability parameter for SU/PG is employed [1]:

$$\tau = \frac{h_a}{2\,\|\mathbf{a}\|} \left(\coth(Pe_a) - \frac{1}{Pe_a} \right). \tag{10}$$

In the above, $Pe_a = \|\mathbf{a}\|\, h_a / 2k$ is the directional grid Péclet number and h_a is a characteristic length, herein taken as the length of a representative nodal domain in the direction of the advection.

The choice of the stabilization parameter for meshfree methods is not straightforward and has been discussed at length in [19]. The use of the classical parameter (10) has been shown to be suitable for RKPM so long as the support parameter is not “large” (e.g. three times the nodal spacing for linear basis) [19].

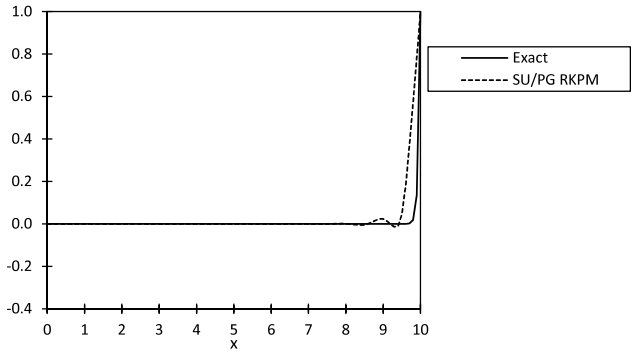

Fig. 2. RKPM with SU/PG stabilization applied to the steady advection–diffusion equation with $Pe_h = 5$.

3. Implicit gradient RKPM for stabilization of convection dominated problems

3.1. Implicit gradient reproducing kernel particle method

In this section we briefly review the reproducing kernel (RK) approximation which is used to construct the trial functions, and introduce the implicit gradient RK approximation for the test functions. Let the closed domain $\bar{\Omega}$ be discretized by a set of NP nodes. The RK approximation $u^h(\mathbf{x})$ of a function $u(\mathbf{x})$ is defined by

$$u^h(\mathbf{x}) = \sum_{I=1}^{NP} \Psi_I(\mathbf{x}) u_I \tag{11}$$

where $\{\Psi_I(\mathbf{x})\}_{I=1}^{NP}$ is the set of RK shape functions with nth order completeness, and $\{u_I\}_{I=1}^{NP}$ is the set of coefficients of the approximation. The RK shape functions are constructed by the product of a kernel function $\Phi_\rho(\mathbf{x} - \mathbf{x}_I)$ and a correction function [12,36]:

$$\Psi_I(\mathbf{x}) = \mathbf{H}^{\mathrm{T}}(\mathbf{x} - \mathbf{x}_I)\mathbf{b}(\mathbf{x})\,\Phi_\rho(\mathbf{x} - \mathbf{x}_I) \tag{12}$$

where $\Phi_\rho(\mathbf{x} - \mathbf{x}_I)$ is a kernel function with compact support measure ρ, $\mathbf{H}(\mathbf{x} - \mathbf{x}_I)$ is the basis vector containing the set of complete nth order monomials

$$\mathbf{H}(\mathbf{x} - \mathbf{x}_I) = \left[1,\ x_1 - x_{1I}, x_2 - x_{2I}, (x_1 - x_{1I})^2, \ldots, (x_2 - x_{2I})^n\right]^{\mathrm{T}}, \tag{13}$$

and $\mathbf{b}(\mathbf{x})$ is a coefficient vector. The kernel function defines the locality and the smoothness of the RK approximation, for example, a cubic B-spline kernel gives C^2 continuity of the approximation. The product of the basis vector and coefficients, $\mathbf{H}^{\mathrm{T}}(\mathbf{x}-\mathbf{x}_I)\mathbf{b}(\mathbf{x})$, is called the correction function, which allows the approximation to reproduce any basis contained in $\mathbf{H}(\mathbf{x} - \mathbf{x}_I)$.

The coefficient vector $\mathbf{b}(\mathbf{x})$ is obtained by enforcing the following reproducing conditions:

$$\sum_{I=1}^{NP} \Psi_I(\mathbf{x}) x_{1I}^i x_{2I}^j = x_1^i x_2^j \quad 0 \le i + j \le n. \tag{14}$$

Substituting (12) into (14), the RK shape functions are constructed as

$$\Psi_I(\mathbf{x}) = \mathbf{H}^{\mathrm{T}}(\mathbf{0})\mathbf{M}(\mathbf{x})^{-1}\mathbf{H}(\mathbf{x} - \mathbf{x}_I)\,\Phi_\rho(\mathbf{x} - \mathbf{x}_I) \tag{15}$$

where

$$\mathbf{M}(\mathbf{x}) = \sum_{I=1}^{NP} \mathbf{H}(\mathbf{x} - \mathbf{x}_I)\mathbf{H}^{\mathrm{T}}(\mathbf{x} - \mathbf{x}_I)\,\Phi_\rho(\mathbf{x} - \mathbf{x}_I) \tag{16}$$

is called the moment matrix, and $\mathbf{H}(\mathbf{0}) = [1, 0, \ldots, 0]^{\mathrm{T}}$.

Table 1
Implicit gradient RKPM vector.

Method	$\tilde{\mathbf{H}}(\mathbf{x})$
SU/PG [1]	$[1, -\tau a_1(\mathbf{x}), -\tau a_2(\mathbf{x}), 0, \ldots, 0]^{\mathrm{T}}$
G/LS [2]	$[1, -\tau a_1(\mathbf{x}), -\tau a_2(\mathbf{x}), -2\tau k, 0, -2\tau k, 0, \ldots, 0]^{\mathrm{T}}$
SGS [3]	$[1, -\tau a_1(\mathbf{x}), -\tau a_2(\mathbf{x}), 2\tau k, 0, 2\tau k, 0, \ldots, 0]^{\mathrm{T}}$

In order to construct the test functions, stabilization must be considered for obtaining a stable solution in the presence of convection dominance, as discussed in the previous sections. However, the approach in (8) of modifying the Bubnov–Galerkin test functions may require up to third order derivatives in the discrete form of the problem. For RKPM, construction of these derivatives can be particularly expensive due to the differentiation of the inverse of the moment matrix $\mathbf{M}(\mathbf{x})^{-1}$ in the RK shape function (15). To avoid the computational expense of calculating these derivatives, the implicit gradient reproducing kernel approximation is introduced. The basic idea for constructing these test functions is to achieve the same form of stabilization in (8) without explicit differentiation. To accomplish this, the following modification to the reproducing condition (14) is introduced to construct the test functions, with the operator $\mathbb{L}$ defined by (7):

$$\sum_{I=1}^{NP} \tilde{\Psi}_I^{\nabla}(\mathbf{x}) x_{1I}^i x_{2I}^j = x_1^i x_2^j + \tau \mathbb{L}(x_1^i x_2^j), \quad 0 \le i + j \le n \tag{17}$$

where $\{\tilde{\Psi}_I^{\nabla}(\mathbf{x})\}_{I=1}^{NP}$ is the set of implicit gradient shape functions to be defined. The reproducing condition (17) can be expressed in a generalized fashion as

$$\sum_{I=1}^{NP} \tilde{\Psi}_I^{\nabla}(\mathbf{x}) x_{1I}^i x_{2I}^j = x_1^i x_2^j + \tau \sum_{p+q=0}^{n} \alpha_{pq}(\mathbf{x}) D_{pq}(x_1^i x_2^j), \quad 0 \le i + j \le n \tag{18}$$

where $D_{pq}(\cdot) = \partial^{p+q}(\cdot)/\partial x_1^p \partial x_2^q$ and the coefficients $\alpha_{pq}(\mathbf{x})$ are straightforwardly determined based on the operator $\mathbb{L}$. Eq. (18) can then be recast as:

$$\sum_{I=1}^{NP} \tilde{\Psi}_I^{\nabla}(\mathbf{x})(x_1 - x_{1I})^i (x_2 - x_{2I})^j = \delta_{i0}\delta_{j0} + \tau \alpha_{ij}(\mathbf{x})(-1)^{i+j} i! j!, \quad 0 \le i + j \le n. \tag{19}$$

Consider now implicit gradient reproducing kernel shape functions in the form of (12):

$$\tilde{\Psi}_I^{\nabla}(\mathbf{x}) = \mathbf{H}^{\mathrm{T}}(\mathbf{x} - \mathbf{x}_I)\tilde{\mathbf{b}}(\mathbf{x})\, \Phi_\rho(\mathbf{x} - \mathbf{x}_I). \tag{20}$$

Using (20) the reproducing condition (19) can be written as:

$$\sum_{I=1}^{NP} \mathbf{H}(\mathbf{x} - \mathbf{x}_I)\mathbf{H}^{\mathrm{T}}(\mathbf{x} - \mathbf{x}_I)\tilde{\mathbf{b}}(\mathbf{x})\, \Phi_\rho(\mathbf{x} - \mathbf{x}_I) = \tilde{\mathbf{H}}(\mathbf{x}) \tag{21}$$

where $\tilde{\mathbf{H}}(\mathbf{x})$ is a vector containing terms from the right hand side of (19). The values in this vector for the three stabilization methods discussed herein are presented in Table 1 for the advection–diffusion equation.

The coefficient vector $\tilde{\mathbf{b}}(\mathbf{x})$ is obtained from (21) as

$$\tilde{\mathbf{b}}(\mathbf{x}) = \mathbf{M}(\mathbf{x})^{-1}\tilde{\mathbf{H}}(\mathbf{x}). \tag{22}$$

Consequently, the IG-RKPM shape function is constructed as:

$$\tilde{\Psi}_I^{\nabla}(\mathbf{x}) = \tilde{\mathbf{H}}^{\mathrm{T}}(\mathbf{x})\mathbf{M}(\mathbf{x})^{-1}\mathbf{H}(\mathbf{x} - \mathbf{x}_I)\, \Phi_\rho(\mathbf{x} - \mathbf{x}_I). \tag{23}$$

Comparing (15) and (23), it can be seen that the first term on the right hand side of (23) is the only modification of the RKPM framework. Stabilization using IG-RKPM is thus very straightforward compared to the explicit version,

and can also be added to existing codes easily with virtually no additional cost. Thus, the method offers both low computational cost, and the simplicity of the standard Bubnov–Galerkin method since no additional terms arise in the discrete form of the problem.

To examine the increased simplicity of IG-RKPM over standard stabilization, consider the test and trial functions approximated in (9) as:

$$\begin{aligned} u^h(\mathbf{x}) &= \sum_{I=1}^{NP} \Psi_I(\mathbf{x}) u_I, \\ \tilde{w}^h(\mathbf{x}) &= \sum_{I=1}^{NP} \tilde{\Psi}_I(\mathbf{x}) w_I, \end{aligned} \tag{24}$$

where Ψ_I is the RK shape function (15), and for IG-RKPM, test functions are constructed from (23) giving $\tilde{\Psi}_I = \tilde{\Psi}_I^{\nabla}$, and for RKPM with SU/PG, test functions are obtained from the relation (8) giving $\tilde{\Psi}_I = \Psi_I + \tau \mathbf{a} \cdot \nabla \Psi_I$. Substituting (24) into (9), the semi-discrete matrix form of the problem is obtained:

$$\mathbf{M}\dot{\mathbf{u}} + \mathbf{K}\mathbf{u} = \mathbf{f}. \tag{25}$$

The matrix definitions in the above for IG-RKPM are given as

$$\begin{aligned} M_{IJ} &= \int_\Omega \tilde{\Psi}_I \, \Psi_J \, \mathrm{d}\Omega, \\ \mathrm{K}_{IJ} &= \int_\Omega k \tilde{\mathbf{B}}_I^{\mathrm{T}} \mathbf{B}_J \, \mathrm{d}\Omega + \int_\Omega \tilde{\Psi}_I \mathbf{A} \mathbf{B}_J \, \mathrm{d}\Omega, \\ \mathrm{f}_I &= \int_\Omega \tilde{\Psi}_I s \, \mathrm{d}\Omega + \int_{\partial\Omega_h} \tilde{\Psi}_I h \, \mathrm{d}\Omega, \end{aligned} \tag{26}$$

where

$$\begin{aligned} \mathbf{B}_I &= \begin{bmatrix} \Psi_{I,x} & \Psi_{I,y} \end{bmatrix}^{\mathrm{T}}, \\ \tilde{\mathbf{B}}_I &= \begin{bmatrix} \tilde{\Psi}_{I,x} & \tilde{\Psi}_{I,y} \end{bmatrix}^{\mathrm{T}}, \\ \mathbf{A} &= \begin{bmatrix} a_1 & a_2 \end{bmatrix}. \end{aligned} \tag{27}$$

For comparison, using RKPM with SU/PG, the matrix definitions in (25) are

$$\begin{aligned} M_{IJ} &= \int_\Omega \Psi_I \, \Psi_J \, \mathrm{d}\Omega + \int_\Omega \tau \mathbf{A} \mathbf{B}_I \, \Psi_J \, \mathrm{d}\Omega, \\ \mathrm{K}_{IJ} &= \int_\Omega k \mathbf{B}_I^{\mathrm{T}} \mathbf{B}_J \, \mathrm{d}\Omega + \int_\Omega \tau k \mathbf{A} \mathbf{D}_I \mathbf{B}_J \, \mathrm{d}\Omega + \int_\Omega \Psi_I \mathbf{A} \mathbf{B}_J \, \mathrm{d}\Omega + \int_\Omega \tau \mathbf{A} \mathbf{B}_I \mathbf{A} \mathbf{B}_J \, \mathrm{d}\Omega, \\ \mathrm{f}_I &= \int_\Omega \Psi_I s \, \mathrm{d}\Omega + \int_\Omega \tau \mathbf{A} \mathbf{B}_I s \, \mathrm{d}\Omega + \int_{\partial\Omega_h} \Psi_I h \, \mathrm{d}\Omega + \int_{\partial\Omega_h} \tau \mathbf{A} \mathbf{B}_I h \, \mathrm{d}\Omega, \end{aligned} \tag{28}$$

where $\mathbf{A}$, $\mathbf{B}_I$, and $\tilde{\mathbf{B}}_I$ are given by (27), and

$$\mathbf{D}_I = \begin{bmatrix} \Psi_{I,xx} & \Psi_{I,xy} \\ \Psi_{I,xy} & \Psi_{I,yy} \end{bmatrix}. \tag{29}$$

Thus, several additional terms need to be constructed for RKPM with SU/PG, which also involves costly higher order differentiation of the approximation functions. For the G/LS and SGS methods, even more matrix terms are necessary, with even higher order derivatives involved, whereas for IG-RKPM, the matrix definitions in (26) remain the same, the only modification being the vector $\tilde{\mathbf{H}}(\mathbf{x})$ in (23).

It can be noted that the construction of reproducing conditions with derivative terms is directly analogous to [34], where implicit gradients were utilized for regularization in strain localization problems, and similar to the work

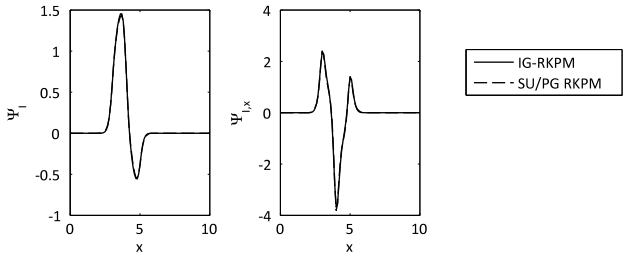

Fig. 3. Comparison of implicit and explicit test functions for the SU/PG method.

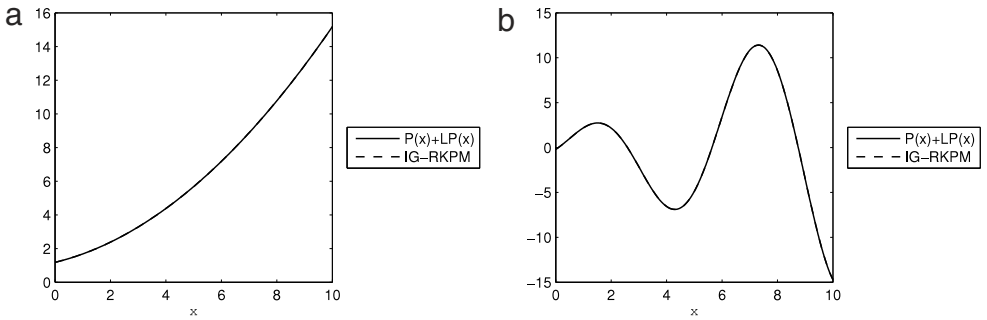

Fig. 4. Implicit gradient and exact solution for (a) $P(x) = 0.1x^2 + 0.2x + 1.0$, and (b) $P(x) = x\ \sin(x)$.

in [35] where derivatives alone were reproduced for the purposes of solving PDEs within the collocation framework. These methods, as well as the present method, follow the ideas originally introduced for synchronized convergence in [32,33].

The proposed shape function for the SU/PG method is plotted in Fig. 3 along with the explicit version for comparison. Here very little difference between the two is observed. In Section 3.3, it is shown that IG-RKPM gives virtually identical results as its explicit counterpart SU/PG RPKM which requires taking explicit second order derivatives of approximation functions in the discrete form for stabilization.

3.2. Properties of implicit gradient representation

The proposed method implicitly includes a portion of the gradient of the shape function by enforcing the gradient reproducing condition (17). Its main characteristic then is the exact reproduction of nth order polynomials in addition to portions of any derivatives. An interesting result is that the resulting approximation space also retains the ability to represent nth order polynomials exactly, and thus may have uses in other applications as a Bubnov–Galerkin approach with gradient reproduction.

To examine the accuracy of the approximation, two functions and the operator $\mathbb{L} = \mathcal{L}$ acting on the function are approximated using IG-RKPM. Constant scalar values $a = 0.1$ and $k = 1.0$ are chosen, and the value of τ is set uniformly to 0.25. For the RK discretization, quadratic bases are employed with quartic B-spline kernels, and a normalized support of 3.0. The length of the domain is chosen as 10.0 and the spacing of the nodes 0.1. The results for both functions are shown in Fig. 4. The first function is $P(x) = 0.1x^2 + 0.2x + 1.0$, and the IG-RKPM method is able to reproduce $P(x) + \mathbb{L}P(x)$ exactly. The second function is $P(x) = x\ \sin(x)$, which is not exactly reproduced, but the error is negligible. It can be seen that the derivatives can be represented without the computational cost of differentiation, especially significant in the case of SGS and G/LS for which third order derivatives show up in the discrete form after introducing stabilization.

To closer examine the properties of the implicit gradient approximation, consider the shape functions (20) with non-shifted bases, for clarity of presentation:

$$\tilde{\Psi}_I^{\nabla}(\mathbf{x}) = \mathbf{H}^{\mathrm{T}}(\mathbf{x}_I)\tilde{\mathbf{b}}(\mathbf{x})\,\Phi_\rho(\mathbf{x} - \mathbf{x}_I). \tag{30}$$

Now consider the reproducing condition (17) which defines the function:

$$\sum_{I=1}^{NP} \tilde{\Psi}_I^{\nabla}(\mathbf{x})\mathbf{H}(\mathbf{x}_I) = \mathbf{H}(\mathbf{x}) + \tau \mathbb{L}\mathbf{H}(\mathbf{x}). \tag{31}$$

Substituting (30) into (31), the IG-RKPM shape function can be expressed as

$$\tilde{\Psi}_I^{\nabla}(\mathbf{x}) = \mathbf{H}^{\mathrm{T}}(\mathbf{x})\hat{\mathbf{M}}^{-1}(\mathbf{x})\mathbf{H}(\mathbf{x}_I)\,\Phi_\rho(\mathbf{x}-\mathbf{x}_I) + \tau \mathbb{L}\mathbf{H}^{\mathrm{T}}(\mathbf{x})\hat{\mathbf{M}}^{-1}(\mathbf{x})\mathbf{H}(\mathbf{x}_I)\,\Phi_\rho(\mathbf{x}-\mathbf{x}_I) \tag{32}$$

where

$$\hat{\mathbf{M}}(\mathbf{x}) = \sum_{I=1}^{NP} \mathbf{H}(\mathbf{x}_I)\mathbf{H}^{\mathrm{T}}(\mathbf{x}_I)\,\Phi_\rho(\mathbf{x}-\mathbf{x}_I) \tag{33}$$

is the moment matrix obtained using non-shifted basis and reproducing conditions (17) directly. Stabilization using explicit differentiation (8) gives the stabilized shape function

$$\begin{aligned}\tilde{\Psi}_I(\mathbf{x}) = {} & \mathbf{H}^{\mathrm{T}}(\mathbf{x})\hat{\mathbf{M}}^{-1}(\mathbf{x})\mathbf{H}(\mathbf{x}_I)\,\Phi_\rho(\mathbf{x}-\mathbf{x}_I) + \tau\Big(\mathbb{L}\mathbf{H}^{\mathrm{T}}(\mathbf{x})\hat{\mathbf{M}}^{-1}(\mathbf{x})\mathbf{H}(\mathbf{x}_I)\,\Phi_\rho(\mathbf{x}-\mathbf{x}_I) \\ & + \mathbf{H}^{\mathrm{T}}(\mathbf{x})\mathbb{L}\hat{\mathbf{M}}^{-1}(\mathbf{x})\mathbf{H}(\mathbf{x}_I)\,\Phi_\rho(\mathbf{x}-\mathbf{x}_I) + \mathbf{H}^{\mathrm{T}}(\mathbf{x})\hat{\mathbf{M}}^{-1}(\mathbf{x})\mathbb{L}\mathbf{H}(\mathbf{x}_I)\,\Phi_\rho(\mathbf{x}-\mathbf{x}_I) \\ & + \mathbf{H}^{\mathrm{T}}(\mathbf{x})\hat{\mathbf{M}}^{-1}(\mathbf{x})\mathbf{H}(\mathbf{x}_I)\mathbb{L}\Phi_\rho(\mathbf{x}-\mathbf{x}_I)\Big).\end{aligned} \tag{34}$$

Comparing (32) to (34), it can be seen that the implicit gradient (32) contains only a specific portion of the full derivative in (34). Utilizing this term as a gradient approximation can be shown to be equivalent to employing diffuse derivatives originally introduced in the diffuse element method (DEM) [37]. An advantage of IG-RKPM, however, is that the implicit gradients are directly embedded in the approximation functions and require less computational and implementation effort. The details showing the equivalence can be found in the Appendix.

3.3. Test of IG-RKPM on the model problem

IG-RKPM with SU/PG is applied to the steady one-dimensional model problem in Section 2 with the same discretization previously employed. The results are shown in Fig. 5 along with RKPM with explicit SU/PG for comparison. It can be seen that virtually identical results are obtained for both methods, while for IG-RKPM, the results are obtained without higher order derivatives necessary to perform stabilization.

4. High order SCNI for convection dominated problems

4.1. Nodal integration in convection dominated problems

Domain integration in meshfree methods needs special attention due to the CPU burden of high-order Gaussian quadrature necessary to ensure solution accuracy. Nodal integration is a natural choice to consider, offers considerable simplicity, and is computationally inexpensive. However this technique can yield non-convergent solutions, and is also subject to instability [26]. The under-integration of the weak form does not provide sufficient accuracy in the solution to give convergent results in many discretizations [26,28]. The instability is due to the underestimation of energy associated with modes of node-to-node oscillations since first derivatives of these modes are zero or near zero at the nodes. SCNI has been introduced in [26] to overcome this difficulty, where nodal integration is employed, but derivatives of the test and trial functions are smoothed over conforming representative nodal domains and the divergence theorem is utilized such that derivatives are not evaluated directly at the nodes:

$$\begin{aligned}\bar{\nabla} u^h(\mathbf{x}_L) &= \frac{1}{A_L}\int_{\partial\Omega_L} u^h(\mathbf{x})\mathbf{n}(\mathbf{x})\,\mathrm{d}\Gamma, \\ \bar{\nabla} \tilde{w}^h(\mathbf{x}_L) &= \frac{1}{A_L}\int_{\partial\Omega_L} \tilde{w}^h(\mathbf{x})\mathbf{n}(\mathbf{x})\,\mathrm{d}\Gamma,\end{aligned} \tag{35}$$

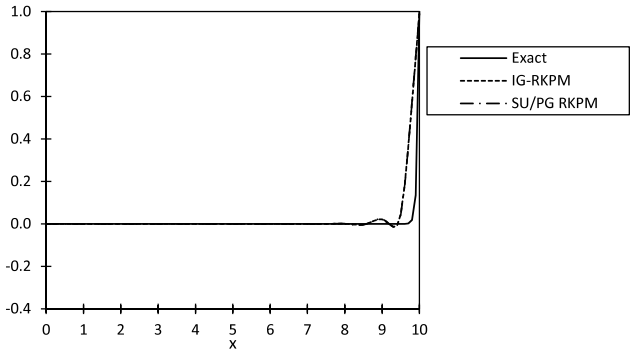

Fig. 5. IG-RKPM and SU/PG RKPM applied to the steady advection–diffusion equation with $Pe_h = 5$.

where $\bar{\nabla}$ denotes the smoothed gradient operator, and $A_L = \int_{\Omega_L} \mathrm{d}\Omega$. Nodal domains Ω_L can be generated by, for example, Voronoi diagrams. The smoothed derivatives in (35) also yield linear Galerkin exactness in second order self-adjoint PDEs, and subsequently give optimal convergence. Further, since nodal integration is employed, the method is also extremely efficient. The combination of these properties makes it more effective than using Gaussian quadrature [26].

Let the test functions $\tilde{w}^h(\mathbf{x})$ be approximated by the implicit gradient shape functions (23), and trial functions $u^h(\mathbf{x})$ be approximated by the RK shape functions (15):

$$\begin{aligned} u^h(\mathbf{x}) &= \sum_{I=1}^{NP} \Psi_I(\mathbf{x}) u_I, \\ \tilde{w}^h(\mathbf{x}) &= \sum_{I=1}^{NP} \tilde{\Psi}_I^{\nabla}(\mathbf{x}) w_I. \end{aligned} \tag{36}$$

Substituting the above approximations and their smoothed gradients (35) into the stabilized Galerkin problem (9), the resulting semi-discrete form for IG-RKPM with SCNI integration is

$$\begin{aligned} &\sum_{L=1}^{NP} \tilde{w}^h(\mathbf{x}_L)\dot{u}^h(\mathbf{x}_L)A_L + \sum_{L=1}^{NP} k\bar{\nabla}\tilde{w}^h(\mathbf{x}_L)\cdot\bar{\nabla}u^h(\mathbf{x}_L)A_L + \sum_{L=1}^{NP} \tilde{w}^h(\mathbf{x}_L)\mathbf{a}(\mathbf{x}_L)\cdot\bar{\nabla}u^h(\mathbf{x}_L)A_L \\ &\quad = \sum_{L=1}^{NP} \tilde{w}^h(\mathbf{x}_L)s(\mathbf{x}_L)A_L + \sum_{L=1}^{NPh} \tilde{w}^h(\mathbf{x}_L)h(\mathbf{x}_L)S_L \end{aligned} \tag{37}$$

where NPh is the number of integration points on the natural boundary, and the terms S_L are the weights of the integration points on the natural boundary. While SCNI is very effective at solving self-adjoint PDEs, the results shown in Fig. 6 for solving the steady one-dimensional model problem in Section 2 with IG-RKPM and SCNI demonstrate that this is not the case for non-self-adjoint problems, as large oscillations appear in the solution.

The reason for the observed oscillations may be explained by the subsequent work on SCNI by Chen, Puso, and colleagues [38,39,30], where it was shown that low-energy spurious oscillatory modes can still exist in the solution under certain conditions. When excited, these modes pollute the solution and effective stabilization is required. The sharp gradient in the solution of the problem may be a source of excitation for these particular modes, and thus strong convection appears to be a setting where SCNI requires additional stabilization. The works in [38,39,30] introduce a stabilization which was shown to preclude the modes, but requires tuning a parameter based on the problem at hand. This method can be traced back to the high order SCNI technique [29] where additional points are added for integration accuracy. The method does not include a stabilization parameter, and can be interpreted as providing additional integration accuracy and subsequent stability. A high order SCNI for the advection–diffusion equation is introduced in the next section to this end.

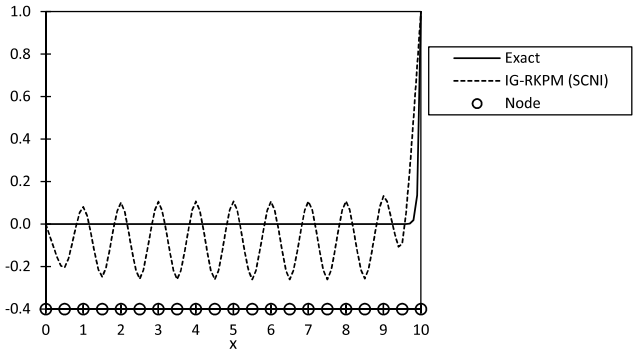

Fig. 6. IG-RKPM with SCNI applied to the steady advection–diffusion equation with $Pe_h = 5$.

4.2. High order SCNI for the advection–diffusion equation

Since higher order integration can avoid the instability due to domain integration shown in the previous section, high order SCNI is proposed for convection dominated problems. For numerical integration of the diffusion term in (9), the form proposed in [29] is

$$\int_\Omega k\nabla\tilde{w}^h \cdot \nabla u^h \,\mathrm{d}\Omega = \sum_{L=1}^{NP} \left\{ k\bar{\nabla}\tilde{w}^h(\mathbf{x}_L) \cdot \bar{\nabla} u^h(\mathbf{x}_L) A_L + \int_{\Omega_L} k(\nabla\tilde{w}^h - \bar{\nabla}\tilde{w}^h(\mathbf{x}_L)) \cdot (\nabla u^h - \bar{\nabla} u^h(\mathbf{x}_L)) \,\mathrm{d}\Omega \right\}. \tag{38}$$

The first term on the right hand side of the above equation is SCNI integration, and the second term provides additional integration accuracy. The equivalence of the right and left hand side can easily be established by expanding the second term in the right hand side and using the definition of the smoothed derivative (35):

$$\begin{aligned} &\sum_{L=1}^{NP} \int_{\Omega_L} k(\nabla\tilde{w}^h - \bar{\nabla}\tilde{w}^h(\mathbf{x}_L)) \cdot (\nabla u^h - \bar{\nabla} u^h(\mathbf{x}_L)) \,\mathrm{d}\Omega \\ &= \sum_{L=1}^{NP} \int_{\Omega_L} k\nabla\tilde{w}^h \cdot \nabla u^h \,\mathrm{d}\Omega - \sum_{L=1}^{NP} \int_{\Omega_L} k\bar{\nabla}\tilde{w}^h(\mathbf{x}_L) \cdot \bar{\nabla} u^h(\mathbf{x}_L) \,\mathrm{d}\Omega \\ &= \int_\Omega k\nabla\tilde{w}^h \cdot \nabla u^h \,\mathrm{d}\Omega - \sum_{L=1}^{NP} k\bar{\nabla}\tilde{w}^h(\mathbf{x}_L) \cdot \bar{\nabla} u^h(\mathbf{x}_L) A_L. \end{aligned} \tag{39}$$

Thus, when evaluated numerically, as the order of quadrature in each nodal domain increases, the accuracy of the integration increases.

In addition, in the limit of convection, HSCNI retains linear exactness due to the additional gradient terms vanishing for linear solutions. Note that HSCNI does not require the test and trial functions to be of the same space, and is thus applicable to Petrov–Galerkin formulations.

The additional integration points inside the nodal domain can be generated using Gaussian quadrature rules in the case of square or rectangular domains. Note that this technique differs from background Gaussian quadrature since it is variationally consistent, and solution accuracy can be achieved with lower order quadrature than would be required with variationally inconsistent Gaussian quadrature [28]. For arbitrary nodal domains, quadrature points can be generated by triangulating Voronoi cells into sub-cells with rules for triangles, as shown in Fig. 7. Here Gaussian quadrature on a background grid is also shown for illustration.

For numerical integration of the advective term in (9), consider the following integration to achieve higher accuracy:

$$\int_\Omega \tilde{w}^h \mathbf{a} \cdot \nabla u^h \,\mathrm{d}\Omega = \sum_{L=1}^{NP} \left\{ \tilde{w}^h(\mathbf{x}_L)\mathbf{a}(\mathbf{x}_L) \cdot \bar{\nabla} u^h(\mathbf{x}_L) A_L + \int_{\Omega_L} (\tilde{w}^h \mathbf{a} - \tilde{w}^h(\mathbf{x}_L)\mathbf{a}(\mathbf{x}_L)) \cdot \nabla u^h \,\mathrm{d}\Omega \right\}. \tag{40}$$

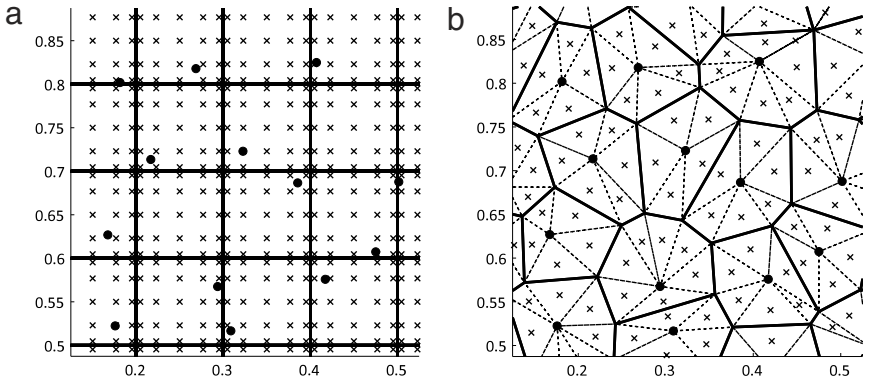

Fig. 7. Example of integration techniques: (a) Gaussian quadrature and (b) HSCNI. Nodes are shown as circles, integration points shown as crosses, integration cells are shown as solid lines, and sub-cells for HSCNI are shown as dashed lines.

The equivalence can be established by expanding the second term in the above equation. Considering the fact that $\tilde{w}(\mathbf{x}_L)\mathbf{a}(\mathbf{x}_L)$ is constant, and using the definition of the smoothed derivative (35) one obtains

$$\begin{aligned}
&\sum_{I=L}^{NP}\int_{\Omega_L}(\tilde{w}^h\mathbf{a}-\tilde{w}^h(\mathbf{x}_L)\mathbf{a}(\mathbf{x}_L))\cdot\nabla u\,\mathrm{d}\Omega\\
&\quad=\sum_{L=1}^{NP}\int_{\Omega_L}\tilde{w}^h\,(\mathbf{a}\cdot\nabla u)\,\mathrm{d}\Omega-\sum_{L=1}^{NP}\tilde{w}^h(\mathbf{x}_L)\mathbf{a}(\mathbf{x}_L)\cdot\int_{\Omega_L}\nabla u^h(\mathbf{x})\,\mathrm{d}\Omega\\
&\quad=\int_{\Omega}\tilde{w}^h\,(\mathbf{a}\cdot\nabla u)\,\mathrm{d}\Omega-\sum_{L=1}^{NP}\tilde{w}^h(\mathbf{x}_L)\mathbf{a}(\mathbf{x}_L)\cdot\bar{\nabla}u(\mathbf{x}_L)A_L.
\end{aligned}\tag{41}$$

As before, because of the equivalence in (40), as the order of quadrature in each cell increases, the accuracy of the integration increases.

Finally, we consider the source terms and unsteady terms in (9), which do not contain smoothed derivatives, integrated with the nodal cell integration introduced:

$$\begin{aligned}
\int_{\Omega_L}\tilde{w}^h\dot{u}^h\,\mathrm{d}\Omega&=\sum_{L=1}^{NP}\int_{\Omega_L}\tilde{w}^h\dot{u}^h\,\mathrm{d}\Omega\\
\int_{\Omega_L}\tilde{w}^h s\,\mathrm{d}\Omega&=\sum_{L=1}^{NP}\int_{\Omega_L}\tilde{w}^h s\,\mathrm{d}\Omega.
\end{aligned}\tag{42}$$

Consider again the steady one-dimensional model problem in Section 2, with the same IG-RKPM discretization as the previous example. HSCNI is employed with two quadrature points per nodal cell. The result shown in Fig. 8 shows that the proposed HSCNI is able to preclude the oscillations present in SCNI for this problem, and only low order quadrature is required for the additional integration accuracy necessary for stability.

Remark. To examine the benefit of the proposed integration in terms of computational cost, one can consider a uniform discretization where nodal domains for HSCNI are box shaped. In this case, in the limit of the discretization, the number of cells for Gaussian integration approaches the number of nodal domains for HSCNI. In [28] it was shown that for linear basis, 5×5 Gaussian quadrature was required to obtain optimal solution accuracy, giving a total of 25 evaluation points per cell for evaluating shape function derivatives. For HSCNI, only four shape function evaluations are necessary to construct the smoothed derivative at the node, and considering 2×2 Gaussian integration in the nodal cell, four evaluations of shape function derivatives are needed for additional stabilizing terms, giving a total of eight points, four of which do not include the CPU intensive meshfree derivatives. Thus the HSCNI proposed offers low computational cost considering the alternative of Gaussian integration.

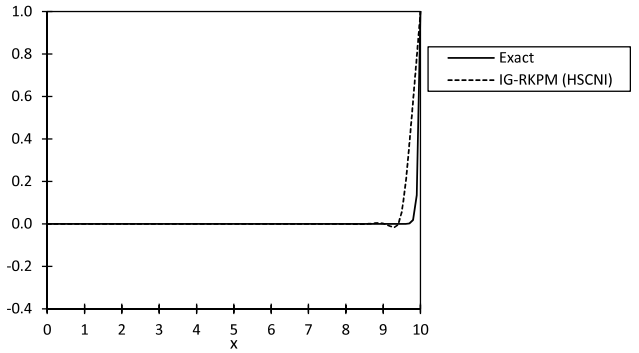

Fig. 8. IG-RKPM with HSCNI applied to the steady advection–diffusion equation with $Pe_h = 5$.

4.3. Semi-discrete matrix form for IG-RKPM with HSCNI

Introducing the RK and implicit gradient approximations (36) for the trial and test functions, respectively, HSCNI using (38), (40) and (42) for domain integration, the matrix form of (9) is expressed as:

$$\mathbf{M}\dot{\mathbf{u}} + \mathbf{K}\mathbf{u} = \mathbf{f} \tag{43}$$

where

$$\begin{aligned}
M_{IJ} &= \sum_{L=1}^{NP} \left\{ \hat{\int}_{\Omega_L} \tilde{\Psi}_I^{\nabla}(\mathbf{x})\, \Psi_J(\mathbf{x})\, \mathrm{d}\Omega \right\}, \\
\mathrm{f}_I &= \sum_{L=1}^{NP} \left\{ \hat{\int}_{\Omega_L} \tilde{\Psi}_I^{\nabla}(\mathbf{x}) s(\mathbf{x})\, \mathrm{d}\Omega \right\} + \hat{\int}_{\partial\Omega_h} \tilde{\Psi}_I^{\nabla}(\mathbf{x}) h(\mathbf{x})\, \mathrm{d}\Gamma, \\
\mathbf{K} &= \mathbf{K}_{\mathrm{diff}} + \mathbf{K}_{\mathrm{adv}}, \\
(\mathrm{K}_{\mathrm{diff}})_{IJ} &= \sum_{L=1}^{NP} \left\{ k\tilde{\bar{\mathbf{B}}}_I^{\mathrm{T}}(\mathbf{x}_L)\bar{\mathbf{B}}_J(\mathbf{x}_L)A_L + \hat{\int}_{\Omega_L} k(\tilde{\mathbf{B}}_I(\mathbf{x}) - \tilde{\bar{\mathbf{B}}}_I(\mathbf{x}_L))^{\mathrm{T}}(\mathbf{B}_J(\mathbf{x}) - \bar{\mathbf{B}}_J(\mathbf{x}_L))\, \mathrm{d}\Omega \right\}, \\
(\mathrm{K}_{\mathrm{adv}})_{IJ} &= \sum_{L=1}^{NP} \left\{ \tilde{\Psi}_I(\mathbf{x}_L)\mathbf{A}(\mathbf{x}_L)\bar{\mathbf{B}}_J(\mathbf{x}_L)A_L + \hat{\int}_{\Omega_L} (\tilde{\Psi}_I(\mathbf{x})\mathbf{A}(\mathbf{x}) - \tilde{\Psi}_I(\mathbf{x}_L)\mathbf{A}(\mathbf{x}_L))\mathbf{B}_J(\mathbf{x})\, \mathrm{d}\Omega \right\},
\end{aligned} \tag{44}$$

the superimposed "$\hat{}$" denotes numerical integration, and

$$\begin{aligned}
\mathbf{B}_I(\mathbf{x}) &= \left[\Psi_{I,x}(\mathbf{x}) \quad \Psi_{I,y}(\mathbf{x}) \right]^{\mathrm{T}}, \\
\bar{\mathbf{B}}_I(\mathbf{x}_L) &= \left[\bar{b}_{I1}^L \quad \bar{b}_{I2}^L \right]^{\mathrm{T}}, \\
\tilde{\mathbf{B}}_I(\mathbf{x}) &= \left[\tilde{\Psi}_{I,x}^{\nabla}(\mathbf{x}) \quad \tilde{\Psi}_{I,y}^{\nabla}(\mathbf{x}) \right]^{\mathrm{T}}, \\
\tilde{\bar{\mathbf{B}}}_I(\mathbf{x}_L) &= \left[\tilde{\bar{b}}_{I1}^L \quad \tilde{\bar{b}}_{I2}^L \right]^{\mathrm{T}}, \\
\bar{b}_{Ii}^L &= \frac{1}{A_L} \hat{\int}_{\partial\Omega_L} \Psi_I(\mathbf{x}) n_i(\mathbf{x})\, \mathrm{d}\Gamma, \\
\tilde{\bar{b}}_{Ii}^L &= \frac{1}{A_L} \hat{\int}_{\partial\Omega_L} \tilde{\Psi}_I^{\nabla}(\mathbf{x}) n_i(\mathbf{x})\, \mathrm{d}\Gamma, \\
\mathbf{A}(\mathbf{x}) &= \left[a_1(\mathbf{x}) \quad a_2(\mathbf{x}) \right].
\end{aligned} \tag{45}$$

The numerical integration of the nodal cell terms can be carried out using low-order quadrature as discussed in Section 4.2, and single point integration can be used to carry out the contour integration necessary for the smoothing terms $\bar{b}_{Ii}^L$ and $\tilde{\bar{b}}_{Ii}^L$ without loss of linear consistency (c.f. [28]).

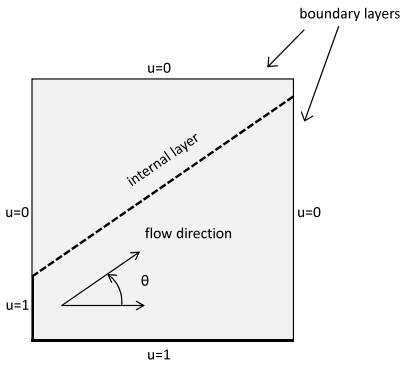

Fig. 9. Problem statement for advection skew to the discretization.

5. Numerical examples

In all numerical examples that follow, RKPM and IG-RKPM with linear basis and quartic B-spline kernels with a normalized support of two are employed. For IG-RKPM, all stabilization methods are identical due to fact that the second order derivatives of the linear bases are zero. For domain integration, HSCNI proposed in Section 4 for the advection–diffusion equation is employed with 2×2 quadrature per nodal cell. The trapezoidal rule is employed for time integration in transient problems. A uniform distribution of 41×41 nodes is employed in all examples. The stabilization parameter for IG-RKPM is taken as (10).

5.1. Advection skew to the discretization with outflow boundary

To test the robustness and streamline properties of IG-RKPM, the two-dimensional steady version of (1) is considered with advection skew to the discretization, as shown in Fig. 9. Here internal and boundary layers exist in the solution. The ability to reasonably represent the internal layer demonstrates proper crosswind diffusion in the numerical solution, and boundary layers also exist for convection dominated flows just as in the one-dimensional case. Constant advection and isotropic diffusion parameters are chosen as $\mathbf{a} = (\cos\theta, \sin\theta)$ and $k = 10^{-6}$ respectively, and the domain is taken to be $[0.0, 1.0] \times [0.0, 1.0]$, so that the flow is convection dominated. The spacing of 0.025 gives a grid Péclet number much larger than unity.

First, the case $\theta = \text{atan}(0.5)$ is considered. The Bubnov–Galerkin RKPM method yields errors that are several orders in magnitude larger than the magnitude in the solution (nearly pure advection of the inflow), as shown in Fig. 10(a). For demonstration purposes, the artificial diffusion that is induced by the advective portion of the operator in SU/PG in the one-dimensional case is added to stabilize the solution. This diffusion is given by $\tilde{k} = \|\mathbf{a}\| h/2$ [1]. Straightforward application results in spurious crosswind diffusion, as seen in Fig. 10(b). The solution with IG-RKPM is shown in Fig. 10(c); comparing the three cases, it is seen that IG-RKPM stabilizes the result, and also shows the streamline property of SU/PG.

Two more challenging cases with larger outflow boundary layers are considered: $\theta = \text{atan}(1.0)$ and $\theta = \text{atan}(2.0)$. The IG-RKPM results for these two cases are shown in Fig. 11, where the method shows good performance in the presence of the fine boundary layers.

5.2. Advection of a cosine hill in a rotating field

A rotating field with advection $\mathbf{a} = (-x_2, x_1)$ on a domain $[-0.5, 0.5] \times [-0.5, 0.5]$ is considered with the steady version of (1), with constant isotropic diffusion is chosen as $k = 10^{-6}$, making the problem one of nearly pure advection. Homogeneous essential boundary conditions are prescribed on the boundary of the domain, and an essential boundary condition of a cosine hill is prescribed along the section A–O shown in Fig. 12:

$$\begin{aligned} &u(\mathbf{x}) = 0.5(\cos(4.0\pi x_2 + \pi) + 1.0) \\ &x_1 = 0.0;\ 0.5 \le x_2 \le 0.0. \end{aligned} \tag{46}$$

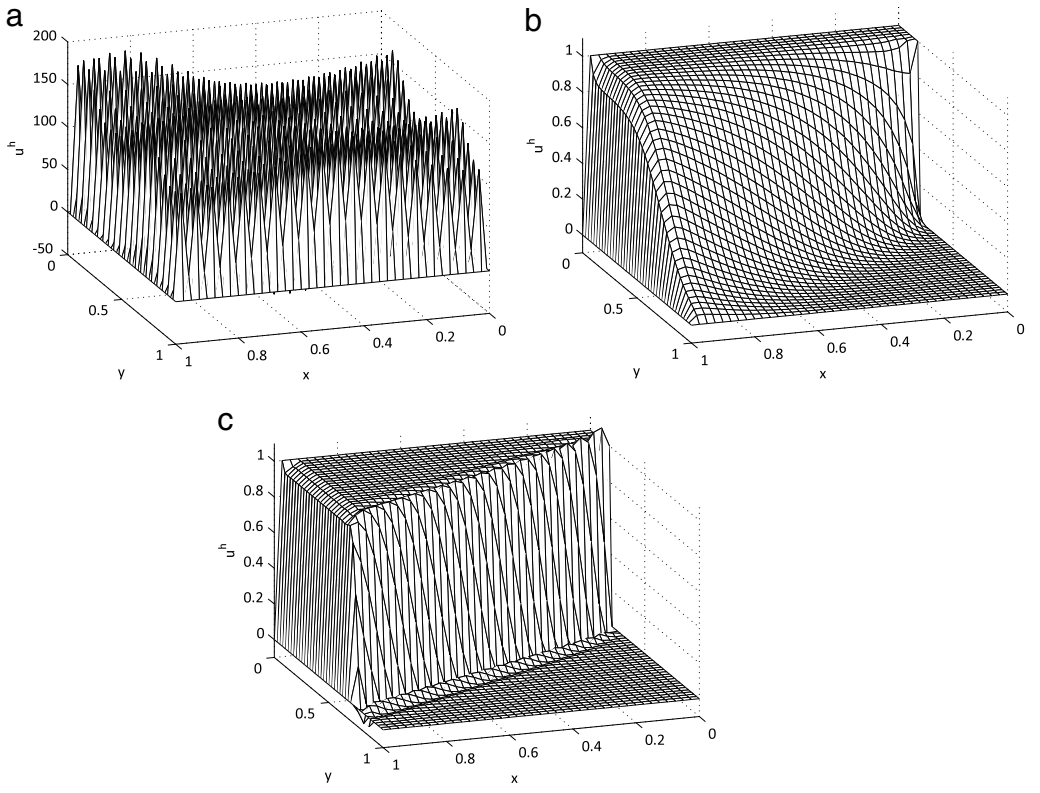

Fig. 10. Examination of crosswind diffusion in advection skew to the discretization with $\theta = \text{atan}(0.5)$; (a) RKPM, (b) artificial diffusion added for stabilization, and (c) IG-RKPM.

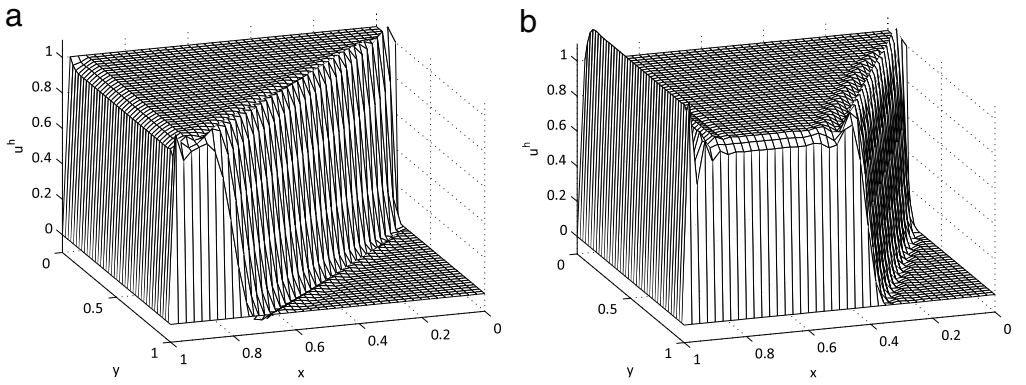

Fig. 11. Advection skew to the discretization with IG-RKPM for (a) $\theta = \text{atan}(1.0)$ and (b) $\theta = \text{atan}(2.0)$.

Standard Bubnov–Galerkin RKPM and the proposed IG-RKPM are applied to the problem. As seen in Fig. 13, both methods give reasonable results, which is expected. However, IG-RKPM gives a smooth solution consistent with the exact solution, while the standard RKPM solution is oscillatory.

5.3. Pure advection of a cone in a rotating field

The rotating advection of a cone illustrates phase error and dissipative error associated with solving advection problems. Errors manifest in this problem as trailing waves and reduction in cone height for phase and dissipative

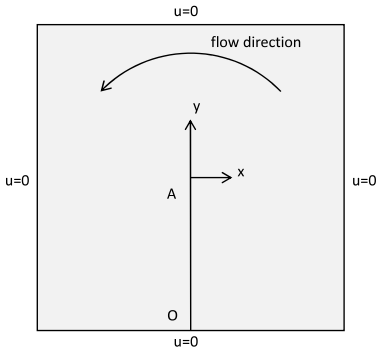

Fig. 12. Problem statement for advection of a cosine hill in a rotating field.

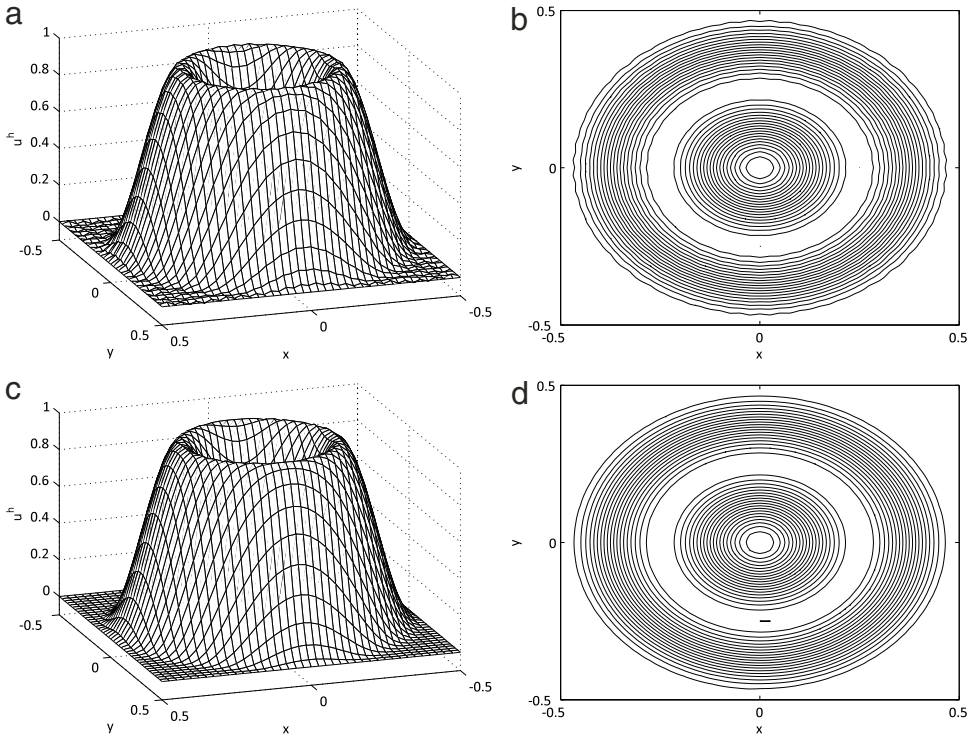

Fig. 13. Advection of a cosine hill in a rotating field: (a) elevation of RKPM result, (b) contours of RKPM result, (c) elevation of IG-RKPM result, and (d) contours of IG-RKPM result. Contours are shown at intervals of 0.05.

error respectively. The problem statement is shown in Fig. 14 where the domain is chosen as $[-0.5, 0.5] \times [-0.5, 0.5]$. The isotropic diffusion constant is zero and the advection velocity is given by $\mathbf{a} = (-x_2, x_1)$. The initial condition is a cone constructed by a cosine hill centered along the line O–A in Fig. 14, with a support of half the length of the segment.

IG-RKPM is employed, along with RKPM for comparison. The results for both methods are shown in Fig. 15 after one rotation. The Bubnov–Galerkin method exhibits virtually no error in dissipation with no loss of cone height, however the phase error is evident by the trailing waves. IG-RKPM also has virtually no error in dissipation with no loss of cone height, but has less phase error with very few trailing waves. In addition, oscillations are seen throughout the domain for RKPM, which is not observed for IG-RKPM.

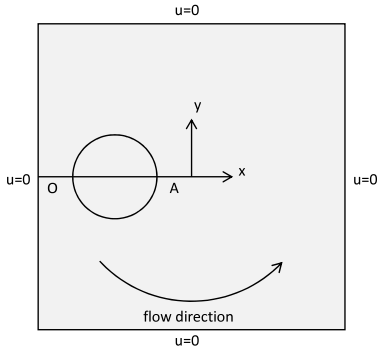

Fig. 14. Problem statement for pure advection of a cone in a rotating field.

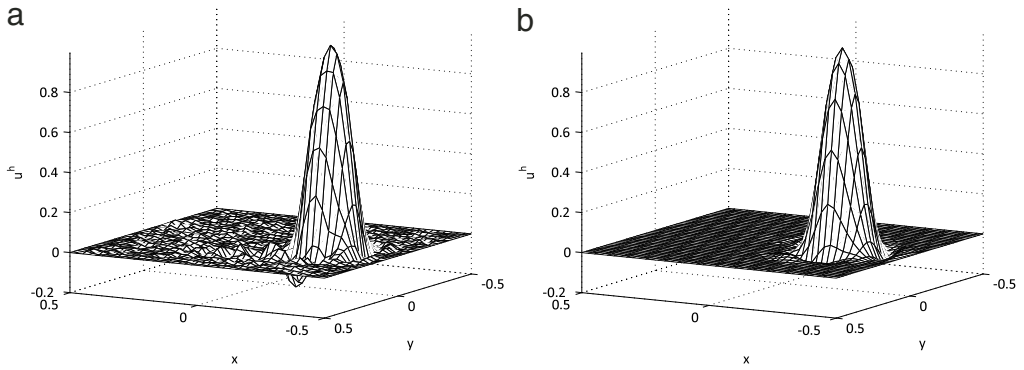

Fig. 15. Rotating cone after a full rotation for (a) RKPM and (b) IG-RKPM.

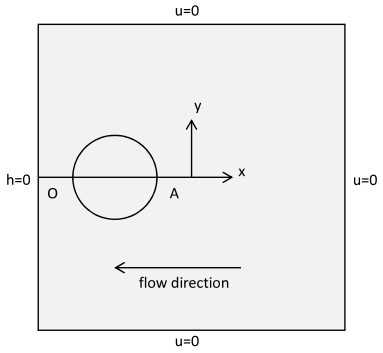

Fig. 16. Problem statement for cone impinging on a natural boundary.

5.4. Cone impinging on a natural boundary

For a cone with a uniform advection velocity $\mathbf{a} = (-1.0, 0.0)$ and a natural outflow boundary condition, the Bubnov–Galerkin formulation exhibits severe oscillations after the cone leaves the domain of interest. The problem statement is shown in Fig. 16, where the same domain and initial conditions as the previous problem are employed. The isotropic diffusion constant is again identically zero.

Bubnov–Galerkin RKPM and IG-RKPM are employed, and the results are shown in Fig. 17 at two time instances. The Bubnov–Galerkin RKPM method performs poorly and exhibits relatively large oscillations after the cone has left the domain, with oscillations about 2.64% of the original cone height. For IG-RKPM, the oscillations are virtually nonexistent (about 10^{-11}% of the original cone height).

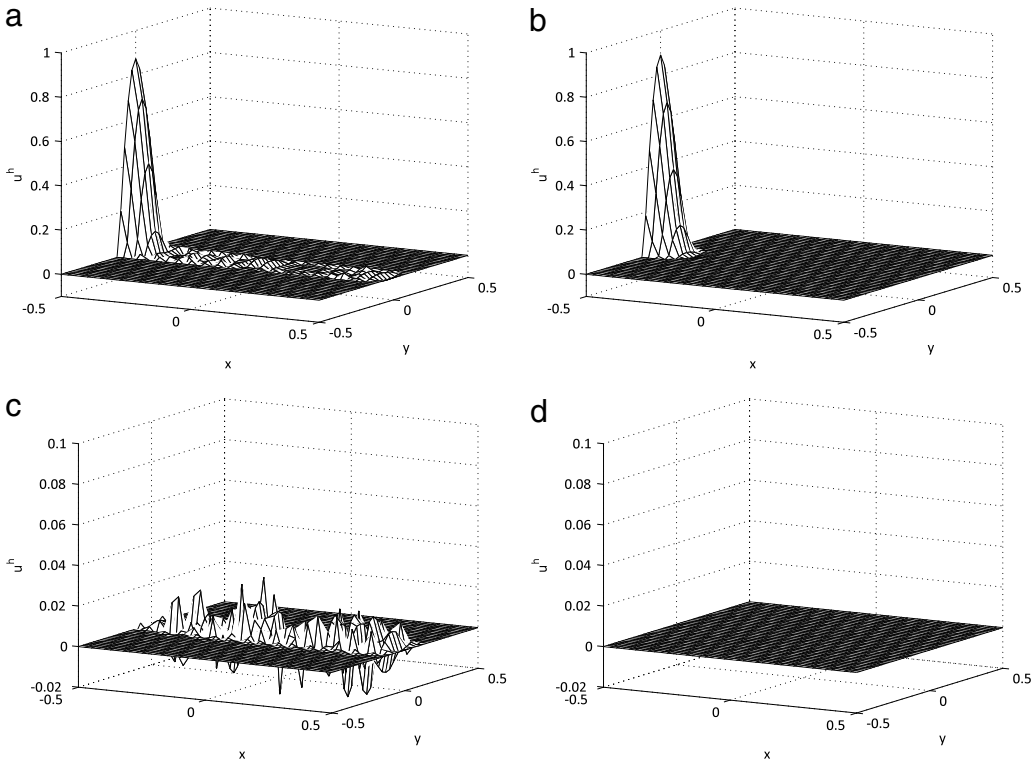

Fig. 17. Cone impinging on natural boundary for (a) RKPM at $t = 0.3$, (b) IG-RKPM at $t = 0.3$, (c) RKPM at $t = 1.0$, and (d) IG-RKPM at $t = 1.0$.

6. Conclusion

In this paper, a new approach to construct a stable RKPM method for convection dominated problems is presented. Gradient terms for the stabilized methods are introduced into the reproducing conditions under a general framework that can include the stabilization in the SU/PG, G/LS, and SGS methods. The implicit inclusion of these terms avoids costly derivatives necessary for constructing the Galerkin form of the problem, and stabilization can be accomplished straightforwardly. It is also shown that the implicit derivatives introduced resemble diffuse derivatives, and retain the desirable properties of true shape function gradients. Domain integration is another issue present in meshfree methods due to the computationally demanding high order quadrature required to ensure solution accuracy. Nodal integration was examined for convection dominated problems; however, SCNI exhibited the instability it was designed to preclude in self-adjoint problems. HSCNI was then introduced for convection dominated problems, which stabilizes the solution, and only requires low order quadrature in the integration cells. The proposed IG-RKPM with HSCNI showed good performance in the steady and transient convection dominated benchmark problems tested.

In general, the IG-RKPM formulation is directly applicable to other PDEs, however there are some cases which need special attention. For example, for the mixed formulation of the incompressible Navier–Stokes equations, IG-RKPM with SU/PG stabilization is nearly identical to the method presented here, but for the SGS and G/LS methods, alternative approaches need to be taken since the implicit inclusion of the pressure field test functions in the velocity field test functions is not straightforward. The extension of the present method to the incompressible Navier–Stokes equations will be considered in future work.

Acknowledgment

The support of this work by US Army Engineer Research and Development Center under contract W912HZ-07-C-0019 is greatly acknowledged.

Appendix. Equivalence of implicit gradients and diffuse derivatives

Consider the moving least squares approximation which is the basis of DEM. First, the weighted least squares approximation in the neighborhood of a location $\bar{\mathbf{x}}$ is [37]:

$$u^h_{\bar{\mathbf{x}}}(\mathbf{x}) = \mathbf{H}^{\mathrm{T}}(\mathbf{x})\mathbf{c}_{\bar{\mathbf{x}}} \tag{47}$$

where $\mathbf{c}_{\bar{\mathbf{x}}}$ is a column vector containing the coefficients of the bases. The coefficients are obtained by minimizing the following expression with respect to $\mathbf{c}_{\bar{\mathbf{x}}}$:

$$J_{\bar{\mathbf{x}}}(\mathbf{c}_{\bar{\mathbf{x}}}) = \sum_{I=1}^{NP} \Phi_\rho(\mathbf{x}-\mathbf{x}_I)\left(\mathbf{H}^{\mathrm{T}}(\mathbf{x}_I)\mathbf{c}_{\bar{\mathbf{x}}} - u_I\right)^2. \tag{48}$$

The moving least squares approximation is obtained by taking $\bar{\mathbf{x}} \to \mathbf{x}$:

$$u^h_{\bar{\mathbf{x}}\to\mathbf{x}}(\mathbf{x}) \equiv u^h_{\mathrm{MLS}}(\mathbf{x}) = \mathbf{H}^{\mathrm{T}}(\mathbf{x})\mathbf{c}_{\mathbf{x}} \tag{49}$$

where

$$\mathbf{c}_{\mathbf{x}} = \hat{\mathbf{M}}^{-1}(\mathbf{x}) \sum_{I=1}^{NP} \mathbf{H}(\mathbf{x}_I)\,\Phi_\rho(\mathbf{x}-\mathbf{x}_I)u_I. \tag{50}$$

The MLS shape functions are obtained by examining (49) and (50):

$$\psi_I(\mathbf{x}) = \mathbf{H}^{\mathrm{T}}(\mathbf{x})\hat{\mathbf{M}}^{-1}(\mathbf{x})\mathbf{H}(\mathbf{x}_I)\,\Phi_\rho(\mathbf{x}-\mathbf{x}_I). \tag{51}$$

Differentiating the basis vector $\mathbf{H}^{\mathrm{T}}(\mathbf{x})$ while assuming the coefficients are constant results in diffuse derivatives:

$$\mathbb{L}\psi_I(\mathbf{x}) \simeq \mathbb{L}\mathbf{H}^{\mathrm{T}}(\mathbf{x})\hat{\mathbf{M}}^{-1}(\mathbf{x})\mathbf{H}(\mathbf{x}_I)\,\Phi_\rho(\mathbf{x}-\mathbf{x}_I). \tag{52}$$

Comparing (52) to (32), it can be seen that the implicit gradient terms are diffuse derivatives of the shape functions.

References

[1] A.N. Brooks, T.J.R. Hughes, Streamline upwind/Petrov–Galerkin formulations for convection dominated flows with particular emphasis on the incompressible Navier–Stokes equations, Comput. Methods Appl. Mech. Engrg. 32 (1982) 199–259.

[2] T.J.R. Hughes, L.P. Franca, G.M. Hulbert, A new finite element formulation for computational fluid dynamics: VIII. The Galerkin/least-squares method for advective-diffusive equations, Comput. Methods Appl. Mech. Engrg. 73 (1989) 173–189.

[3] L.P. Franca, S.L. Frey, T.J.R. Hughes, Stabilized finite element methods: I. Application to the advective-diffusive model, Comput. Methods Appl. Mech. Engrg. 95 (1992) 253–276.

[4] T.J.R. Hughes, Multiscale phenomena: Green's functions, the Dirichlet-to-Neumann formulation, subgrid scale models, bubbles and the origins of stabilized methods, Comput. Methods Appl. Mech. Engrg. 127 (1995) 387–401.

[5] T.J.R. Hughes, G.R. Feijóo, L. Mazzei, J.B. Quincy, The variational multiscale method—a paradigm for computational mechanics, Comput. Methods Appl. Mech. Engrg. 166 (1998) 3–24.

[6] F. Brezzi, A. Russo, Choosing bubbles for advection–diffusion problems, Math. Models Methods Appl. Sci. 4 (1994) 571–587.

[7] L.P. Franca, C. Farhat, Bubble functions prompt unusual stabilized finite element methods, Comput. Methods Appl. Mech. Engrg. 123 (1995) 299–308.

[8] F. Brezzi, M.O. Bristeau, L.P. Franca, M. Mallet, G. Rogé, A relationship between stabilized finite element methods and the Galerkin method with bubble functions, Comput. Methods Appl. Mech. Engrg. 96 (1992) 117–129.

[9] C. Baiocchi, F. Brezzi, L.P. Franca, Virtual bubbles and Galerkin-least-squares type methods (Ga. LS), Comput. Methods Appl. Mech. Engrg. 105 (1993) 125–141.

[10] C. Johnson, U. Nävert, J. Pitkäranta, Finite element methods for linear hyperbolic problems, Comput. Methods Appl. Mech. Engrg. 45 (1984) 285–312.

[11] J. Douglas, J.P. Wang, An absolutely stabilized finite element method for the Stokes problem, Math. Comp. 52 (1989) 495–508.

[12] W.K. Liu, S. Jun, Y.F. Zhang, Reproducing kernel particle methods, Internat. J. Numer. Methods Fluids 20 (1995) 1081–1106.

[13] E. Onate, S. Idelsohn, O.C. Zienkiewicz, R.L. Taylor, A finite point method in computational mechanics. Applications to convective transport and fluid flow, Internat. J. Numer. Methods Engrg. 39 (1996) 3839–3866.

[14] E. Onate, S. Idelsohn, O.C. Zienkiewicz, R.L. Taylor, C. Sacco, A stabilized finite point method for analysis of fluid mechanics problems, Comput. Methods Appl. Mech. Engrg. 139 (1996) 315–346.

[15] S. Atluri, S. Shen, The Meshless Local Petrov–Galerkin (MLPG) Method, Tech Science Press, Encino, California, 2002.

[16] H. Lin, S.N. Atluri, Meshless local Petrov–Galerkin (MLPG) method for convection diffusion problems, Comput. Model. Eng. Sci. 1 (2000) 45–60.
[17] F. Günther, W.K. Liu, D. Diachin, M.A. Christon, Multi-scale meshfree parallel computations for viscous. Compressible flows, Comput. Methods Appl. Mech. Engrg. 190 (2000) 279–303.
[18] T.P. Fries, H.G. Matthies, A Review of Petrov–Galerkin Stabilization Approaches and An Extension to Meshfree Methods, Technische Universitat Braunschweig, Brunswick, 2004.
[19] T.P. Fries, H.G. Matthies, A stabilized and coupled meshfree/meshbased method for the incompressible Navier–Stokes equations—part I: stabilization, Comput. Methods Appl. Mech. Engrg. 195 (2006) 6205–6224.
[20] A. Huerta, S. Fernández-Méndez, Time accurate consistently stabilized mesh-free methods for convection dominated problems, Internat. J. Numer. Methods Engrg. 56 (2003) 1225–1242.
[21] L. Zhang, J. Ouyang, X. Wang, X. Zhang, Variational multiscale element-free Galerkin method for 2D Burgers' equation, J. Comput. Phys. 229 (2010) 7147–7161.
[22] L. Zhang, J. Ouyang, X. Wang, X. Zhang, W. Zhang, On a multi-scale element-free Galerkin method for the Stokes problem, Appl. Math. Comput. 203 (2008) 745–753.
[23] L. Zhang, J. Ouyang, X. Zhang, On a two-level element-free Galerkin method for incompressible fluid flow, Appl. Numer. Math. 58 (2009) 1894–1904.
[24] L. Zhang, J. Ouyang, X. Zhang, The two-level element free Galerkin method for MHD flow at high Hartmann numbers, Phys. Lett. A 372 (2008) 5625–5638.
[25] J. Dolbow, T. Belytschko, Numerical integration of the Galerkin weak form in meshfree methods, Comput. Mech. 23 (1999) 219–230.
[26] J.S. Chen, C.T. Wu, S. Yoon, Y. You, A stabilized conforming nodal integration for Galerkin mesh-free methods, Internat. J. Numer. Methods Engrg. 50 (2001) 435–466.
[27] J.S. Chen, S. Yoon, C.T. Wu, Nonlinear version of stabilized conforming nodal integration for Galerkin meshfree methods, Internat. J. Numer. Methods Engrg. 53 (2002) 2587–2615.
[28] J.S. Chen, M. Hillman, M. Rüter, An arbitrary order variationally consistent integration method for Galerkin meshfree methods, Internat. J. Numer. Methods Engrg. 95 (2013) 387–418.
[29] J.S. Chen, W. Hu, M. Puso, Orbital HP-clouds for solving Schrödinger equation in quantum mechanics, Comput. Methods Appl. Mech. Engrg. 196 (2007) 3693–3705.
[30] M. Puso, J.S. Chen, E. Zywicz, W. Elmer, Meshfree and finite element nodal integration methods, Internat. J. Numer. Methods Engrg. 74 (2008) 416–446.
[31] M. Hillman, J.S. Chen, S.W. Chi, Stabilized and variationally consistent nodal integration for meshfree modeling of impact problems, Comput. Part. Mech. 1 (2014) 245–256.
[32] S. Li, W.K. Liu, Reproducing kernel hierarchical partition of unity Part I: Formulation and theory, Internat. J. Numer. Methods Engrg. 45 (1999) 251–288.
[33] S. Li, W.K. Liu, Reproducing kernel hierarchical partition of unity Part II: Applications, Internat. J. Numer. Methods Engrg. 45 (1999) 289–317.
[34] J.S. Chen, X. Zhang, T. Belytschko, An implicit gradient model by a reproducing kernel strain regularization in strain localization problems, Comput. Methods Appl. Mech. Engrg. 193 (2004) 2827–2844.
[35] S.W. Chi, J.S. Chen, H.Y. Hu, J.P. Yang, A gradient reproducing kernel collocation method for boundary value problems, Internat. J. Numer. Methods Engrg. 93 (2013) 1381–1402.
[36] J.S. Chen, C. Pan, C.T. Wu, W.K. Liu, Reproducing kernel particle methods for large deformation analysis of nonlinear structures, Comput. Methods Appl. Mech. Engrg. 139 (1996) 195–227.
[37] B. Nayroles, G. Touzot, P. Villon, Generalizing the finite element method: diffuse approximation and diffuse elements, Comput. Mech. 10 (1992) 307–318.
[38] J.S. Chen, W. Hu, M.A. Puso, Y. Wu, X. Zhang, Strain smoothing for stabilization and regularization of Galerkin meshfree methods, in: M. Griebel, M.A. Schweitzer (Eds.), Meshfree Methods for Partial Differential Equations III, Springer, Berlin, Heidelberg, 2007, pp. 57–75.
[39] M.A. Puso, E. Zywicz, J.S. Chen, A new stabilized nodal integration approach, in: M. Griebel, M.A. Schweitzer (Eds.), Meshfree Methods for Partial Differential Equations III, Springer, Berlin, Heidelberg, 2007, pp. 207–217.